

Article

Molecular Dynamics Study on the Effect of SiO₂/Al₂O₃ Mass Ratio on the Structural Properties and Viscosity of Molten Fused Red Mud

Bo Xu, Yaran Cao, Zhengzheng Wang, Peipei Du and Yue Long *

School of Metallurgy and Energy, North China University of Science and Technology, Tangshan 063009, China; boxuchina@163.com (B.X.); acaoyaran@163.com (Y.C.); zheng1225764712@163.com (Z.W.); 1710508@stu.neu.edu.cn (P.D.)

* Correspondence: longyue@ncst.edu.cn

Abstract: In this study, molecular dynamics simulation was used to study the effect of SiO₂/Al₂O₃ mass ratio on the structural properties and viscosity of molten fused red mud. The stability of various T–O bonds in the melt was elucidated by analyzing the bond angle and coordination number; the degree of polymerization, and the stability of the melt were explored by analyzing the number of T–O–T bridging oxygen (BO) and the distribution of Q_{Si}^n and Q_{Al}^n of [SiO₄]^{4−} as well as that of Q_{Si}^n and Q_{Al}^n of [AlO₄]^{5−}; the self-diffusion coefficient of each atom was determined by mean square displacement (MSD) analysis; and the trend of the melt viscosity was analyzed according to the relationship between diffusion and viscosity. The results show that as the ratio of SiO₂/Al₂O₃ increases, the viscosity of molten fused red mud first increases, then decreases, and finally increases. This is because Ti⁴ and Fe³⁺ combine with O^{2−} to form [TiO₆]^{8−} octahedron and [FeO₄]^{5−} tetrahedra, which increase the degree of depolymerization of the melt.



Citation: Xu, B.; Cao, Y.; Wang, Z.; Du, P.; Long, Y. Molecular Dynamics Study on the Effect of SiO₂/Al₂O₃ Mass Ratio on the Structural Properties and Viscosity of Molten Fused Red Mud. *Minerals* **2022**, *12*, 925. <https://doi.org/10.3390/min12080925>

Academic Editor: Rajesh Kumar Jyothi

Received: 10 June 2022

Accepted: 19 July 2022

Published: 22 July 2022

Publisher's Note: MDPI stays neutral with regard to jurisdictional claims in published maps and institutional affiliations.



Copyright: © 2022 by the authors. Licensee MDPI, Basel, Switzerland. This article is an open access article distributed under the terms and conditions of the Creative Commons Attribution (CC BY) license (<https://creativecommons.org/licenses/by/4.0/>).

Keywords: fused red mud; molecular dynamics; bridging oxygen; viscosity; SiO₂/Al₂O₃ mass ratio

1. Introduction

Fused red mud is the slag formed after iron extraction from red mud (a solid waste formed in the production of alumina) by a rotary hearth furnace. The production of each ton of alumina generates 0.7 to 2.0 tons of red mud [1,2]. It was estimated that the annual red mud emission in 2018 was over 160 tons worldwide with about 105 million tons disposed in China [3]. Fused red mud contains large amounts of inorganic substances and heavy metals, such as CaO, Na₂O, As, Cr, Cd, etc. The mass storage of fused red mud is potentially a severe safety hazard and may result in pollution, environmental damage, and a very large waste of resources. Over the past few decades, many methods have been adopted to dispose of red mud. For example, red mud can be used to improve thermal stability and mechanical properties of cement-based grouting materials as well as shorten the setting time and enhance the strength of these materials [4–7]. Additionally, red mud can be added to asphalt mixtures to improve the asphalt performance, bulk density, and rutting resistance [8]. Moreover, red mud can be used as a filler to improve the properties of polyvinyl chloride (PVC) [9] and sisal/polyester composites [10]. Finally, continuous glass fiber can be produced from gold tailings, waste limestone, red mud, and ferronickel slag [11].

Fused red mud is categorized as a silicate and mainly consists of SiO₂, Al₂O₃, MgO, and CaO. The use of red mud to prepare high-quality asbestos fibers is an effective method for recovering red mud. Studies on slag have made great progress. For example, Guo et al. studied the effect of MgO/Al₂O₃ ratio (from 0.2 to 0.54) and CaO/SiO₂ ratio (from 1.05 to 1.35) on the CaO–SiO₂–Al₂O₃–MgO–TiO₂ slag system. It was found that increasing the MgO/Al₂O₃ ratio reduced the liquidus temperature, deformation temperature, flow

temperature, and breakpoint temperature, while the CaO/SiO₂ ratio had little effect [12]. Ma et al. added TiO₂ to the CMASTF slag system and found that the viscosity first decreased and then increased as the content of TiO₂ increased [13]. Liu et al. systematically studied the effects of BaO, MnO, and CaO on the CaO–SiO₂–MgO–Al₂O₃–BaO–MnO slag system. They found that the viscosity of the slag system first increased and then decreased with increasing BaO content; the viscosity decreased with the addition of MnO and CaO [14,15]. As the MgO content in the MgO–Al₂O₃–TiO₂–CaO–SiO₂ slag system increased, the viscosity of the slag system decreased, and the fluidity increased [16]. B₂O₃ can increase the degree of polymerization of the CaO–SiO₂–Al₂O₃–MgO (CSAM) system, while Na₂O, K₂O, and MnO have the opposite effect [17]. CaF₂ can facilitate the depolymerization of the silicate network and reduce the melting temperature, viscosity, and viscosity activation energy of the glass [18].

Because of the high temperature of molten slag, its atomic motion state is difficult to observe with conventional methods. Studies have shown that molecular dynamics can be useful for studying molten slag, silicate, glass, etc. Zhang et al. [19] used molecular dynamics to study the relationship between the structure and viscosity of the CaO–SiO₂–Al₂O₃–MgO–TiO₂ slag system. They found that the degree of SiO₂ polymerization is the main factor affecting the viscosity. Mongalo et al. [20] simulated the structure and conductivity of CaO–MgO–Al₂O₃–SiO₂ and found that the conductivity can be predicted well under conditions of low basicity. Zhao et al. [21] studied the effect of CaO/Al₂O₃ ratio on ladle furnace refining slag. They found that the addition of CaO could introduce charge compensators to promote the polymerization of the slag system, thereby increasing the viscosity of the system. Jiang et al. [22] studied the effects of CaO and MgO on the structure and properties of blast furnace ash and reported that CaO improved the viscosity of blast furnace ash significantly more than MgO. Gao et al. [23] studied the effect of CaO/Na₂O ratio on the diffusivity and melting behavior of slag in the SiO₂–Al₂O₃–CaO–Na₂O system by a new method, ring statistics. Dai et al. [24] studied the effect of CaO on the fusion properties of coal ash and found that CaO could reduce the melting point of coal ash and increase its molten fluidity. Atila et al. [25,26] studied the effects of Al₂O₃ on the thermodynamics, elastic properties, and structure of silicate glasses. They found that increasing the Al₂O₃ content could increase the population of bridging oxygen (BO) and oxygen triclusters, glass transition temperature, and elastic modulus. Jabraoui et al. [27] found that increasing the SiO₂ content in silica calcium aluminosilicate glasses reduced the corresponding elastic constants. Fe ions reduced the degree of polymerization of the CaO–SiO₂–Fe_tO system. Na₂O–Al₂O₃–SiO₂ alkali aluminosilicate glass had the best network connectivity when the Al/Na ratio was 1.2 [28,29].

At present, there are few molecular dynamics studies on fused red mud in the molten state. On the other hand, the microstructural properties and viscosity of molten red mud critically influence the quality of the prepared asbestos fibers. Therefore, in this study, the effect of SiO₂/Al₂O₃ ratio on the structural properties and viscosity of molten red mud was simulated by molecular dynamics. This work provides theoretical guidance for the preparation of asbestos fibers from fused red mud.

2. Simulation Method

The key to the success of the molecular dynamics simulation of fused red mud is to select the appropriate potential form and parameters. The Garofalini potential function was used in this study. The Garofalini potential function is composed of a modified Born–Mayer–Huggins (BMH) potential function and a three-body potential function [30]. The modified BMH potential contains a short-range repulsive term and a modified Coulomb term. The resulting BMH potential function is:

$$V_{ij} = \frac{q_i q_j}{4\pi\epsilon_0 r_{ij}} + A_{ij} \exp(-B_{ij} r_{ij}) - \frac{C_{ij}}{r_{ij}^6} - \frac{D_{ij}}{r^8} \quad (1)$$

The first term in the formula represents the Coulomb potential. The molecular dynamics calculation takes into account the interactions not only between any two atoms with residual charges within the cell but also between two atoms with residual charges across cells. The second term in the formula is the short-range repulsive term. The influence of repulsion cannot be ignored in the potential function. Repulsion here mainly refers to the overlap between electron clouds and the electrostatic interaction between nuclei; both can increase the potential energy of the system. The last two terms in the formula represent the attractive potential. The polarization term in the potential function can be neglected. A_{ij} is the charge of atoms i and j . B_{ij} , C_{ij} , and D_{ij} are potential parameters. The potential parameters used in this study are listed in Table 1 [26,31,32].

Table 1. Potential parameters in this study.

i	j	A_{ij} (eV)	B_{ij} (1/Å)	C_{ij} (eV·Å ⁶)
O	O	1.18×10^5	7.31	0
Si	Si	8.32×10^5	8.77	2.75×10^1
Ca	Ca	2.55×10^5	4.68	0
Fe	Fe	8.49×10^5	6.89	0
Mg	Mg	4.16×10^5	6.75	6.91×10^1
O	Si	1.98×10^5	5.77	0
O	Ca	1.52×10^5	4.93	0
O	Fe	2.74×10^5	6.08	0
O	Mg	1.06×10^5	4.95	0
Si	Ca	2.43×10^5	5.52	7.65×10^0
Si	Fe	5.79×10^5	6.64	6.56×10^1
Si	Mg	5.86×10^5	7.64	4.65×10^1
Ca	Fe	4.19×10^5	5.68	0
Ca	Mg	1.82×10^5	5.08	0
Fe	Mg	2.52×10^5	5.59	0
Al	Al	2.44×10^3	3.65	0
Ti	Ti	3.52×10^4	6.25	0
Na	Na	1.35×10^3	6.25	0
Al	O	1.95×10^3	3.55	0
Ti	O	2.40×10^5	6.06	0
Na	O	1.99×10^3	6.25	0
Na	Si	1.25×10^3	6.25	0

In the simulation, the number of atoms of different elements was set according to the mass percentage of various components (Table 2). To ensure that the samples have similar initial conditions, the total numbers of atoms should be as similar as possible. Cubic simulation boxes with a side dimension of 32.5 Å (see Figure 1) were constructed consisting of no less than 2260 and no more than 2280 atoms. The numbers of each atom in the system are listed in Table 3, and the density was set to 2.90 g/cm³.

Table 2. Composition of red mud and number of atoms.

Sample No.	Weight Percentage							$\frac{\text{SiO}_2}{\text{Al}_2\text{O}_3}$
	SiO ₂	Al ₂ O ₃	CaO	MgO	Na ₂ O	Fe ₂ O ₃	TiO ₂	
1#	25	35	12	10	6	8	4	0.71
2#	30	30	12	10	6	8	4	1
3#	35	25	12	10	6	8	4	1.4
4#	40	20	12	10	6	8	4	2
5#	45	15	12	10	6	8	4	3
6#	50	10	12	10	6	8	4	5
7#	55	5	12	10	6	8	4	11

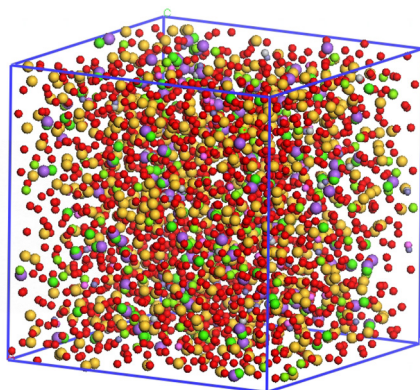


Figure 1. Cubic box of a molten red mud system.

Table 3. Number of atoms in molecular dynamics.

Sample No.	Number of Atoms								
	Ca	Si	Al	Ti	Mg	Fe	Na	O	Total
1#	107	208	344	25	125	38	96	1319	2262
2#	107	250	294	25	125	38	96	1328	2263
3#	107	292	246	25	125	38	96	1340	2269
4#	107	338	196	25	125	38	96	1347	2272
5#	107	375	148	25	125	38	96	1359	2273
6#	107	417	98	25	125	38	96	1368	2274
7#	107	458	50	25	125	38	96	1378	2277

All simulations were performed in an NVT ensemble with a Nose–Hoover thermostat to ensure that the number of atoms, the volume, and the temperature remained constant throughout the simulation. The initial temperature was set to 5000 K, followed by 30 ps of relaxation to obtain a system with uniform particles. Then, the system was cooled to 2000 K in 30 ps at a cooling rate of 1×10^{14} K/s, followed by 30 ps of relaxation at 2000 K. Finally, the system was further cooled to 1800 K in 20 ps at a cooling rate of 1×10^{13} K/s, followed by 30 ps of relaxation at 1800 K (see Figure 2). This ensured that the atoms in the system were evenly mixed and the system was kept in the molten state.

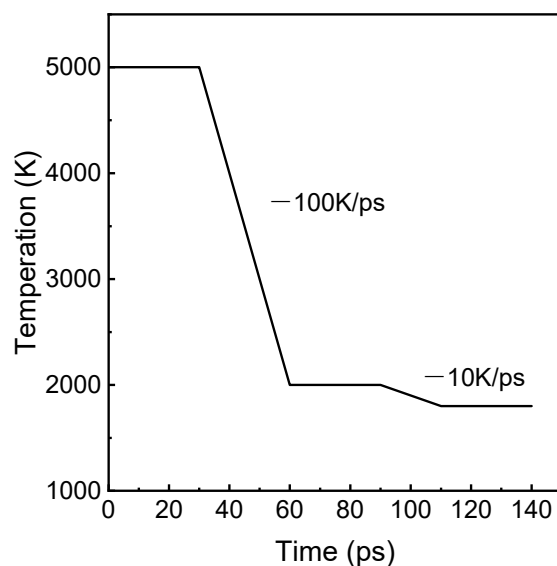


Figure 2. Computing process of simulation.

3. Results and Discussion

3.1. Partial Radial Distribution Function (PDF) and Coordination Number (CN)

The PDF, $g_{ij}(r)$ is generally used to assess the short-range order in the metallurgical slags at high temperature which belongs to an amorphous system. The PDF can be calculated by Equation (2), where N_i and N_j are the total numbers of ions i and j , respectively, V is the volume of the system, and $n(r)$ denotes the average number of the ions j surrounding the ion i in a spherical shell within $r \pm \Delta r/2$. The average coordination number (CN), given by Equation (3), can be evaluated by integrating the $g_{ij}(r)$ curve to its first valley.

$$g_{ij}(r) = \frac{V}{N_i N_j} \sum_j \frac{\langle n_{ij}(r - \Delta r/2, r + \Delta r/2) \rangle}{4\pi r^2 \Delta r} \quad (2)$$

$$N_{ij} = 4\pi \frac{N_j}{V} \int_0^r g_{ij}(r) r^2 dr \quad (3)$$

Figure 3a shows the PDF curves of Si–O, Al–O, Ca–O, Mg–O, Na–O, Ti–O, and Fe–O of the fused red mud sample #1. The first peak of the curve indicates the average bond length between the two atoms. The bond lengths for different pairs are 1.59 Å, 1.79 Å, 2.31 Å, 2.29 Å, 2.33 Å, 2.45 Å, and 2.51 Å, respectively. The calculated results are consistent with those previously determined by molecular dynamics simulations and experiments [33–36]. The bond lengths of Si–O and Al–O are similar and much smaller than those of Ca–O and Mg–O. Compared with other T–O (T = Al, Ca, Mg, Na, Ti, and Fe) bonds, the Si–O bond shows the strongest first peak, indicating that the Si–O bond is the most stable.

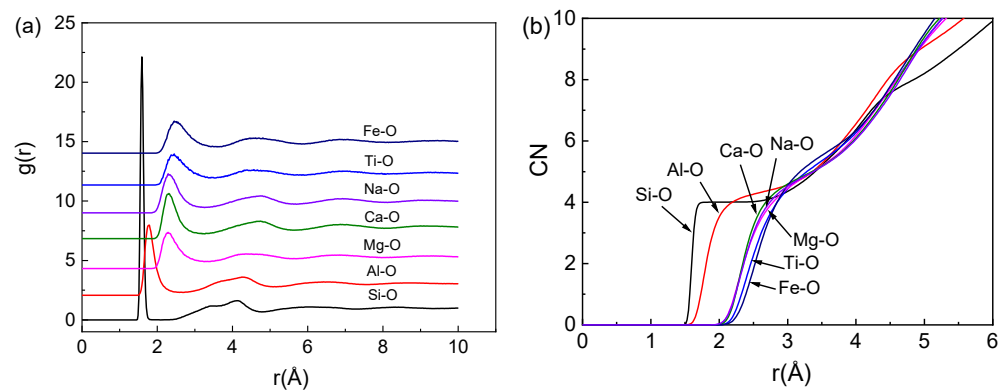


Figure 3. (a) PDF and (b) CN of sample #1 in the fused red mud system.

Figure 3b shows the CNs of different atom pairs in the sample. The value corresponding to the CN platform is the average coordination number. The CN of Si–O remains basically unchanged at approximately 4. The CN platform of Al–O is not as flat as that of Si–O, suggesting that the Al–O bond is slightly less stable than the Si–O bond. Except for Si–O and Al–O, the other T–O bonds do not form platforms, indicating that these T–O bonds do not form a stable network structure.

3.2. Distribution of Bond Angles

There are two types of bond angles in the fused red mud. One is the O–T–O (T = Si, Al) bond angle in the tetrahedron, and the other is the T–O–T bond angle by which the tetrahedra are connected to each other in the network. The shape characteristic of the tetrahedral structure can be determined by the distribution of O–T–O bond angles. The T–O–T bond angle represents the direction in which the tetrahedra are connected in the glass network structure. The flexibility of the T–O–T bond angle determines the degree of disorder of the melt, and it varies in a wide range (approximately 120–180°). The change in the distribution of the T–O–T bond angle indicates whether the structure has become more ordered or disordered.

Figure 4a shows that with increasing $\text{SiO}_2/\text{Al}_2\text{O}_3$ ratio, the peak value of the O–Si–O bond angle distribution increases, and the peak width decreases. The bond angle is approximately 110.2° , and the theoretical bond angle of tetrahedral O–Si–O is 109.5° [36,37]. The result suggests that the structure of $[\text{SiO}_4]^{4-}$ becomes more stable with increasing $\text{SiO}_2/\text{Al}_2\text{O}_3$ ratio. Figure 4b shows the distribution of the O–Al–O bond angle in the aluminum oxide tetrahedron. The bond angle is approximately 106.5° , and the peak is wider than that of O–Si–O, indicating that $[\text{AlO}_4]^{5-}$ has a more regular shape but slightly lower stability than $[\text{SiO}_4]^{4-}$. Figure 4c shows the Si–O–Si bond angle distribution. The bond angle is approximately 144.5° . The width of the peak gradually decreases as the $\text{SiO}_2/\text{Al}_2\text{O}_3$ ratio increases, indicating that more $[\text{SiO}_4]^{4-}$ tetrahedra are connected with each other and that the degree of order increases. Figure 4d shows the distribution of the Al–O–Si bond angle. The bond angle is approximately 138.9° . As the $\text{SiO}_2/\text{Al}_2\text{O}_3$ ratio increases, the peak intensity gradually decreases, but the peak width becomes larger, indicating that the connection between $[\text{SiO}_4]^{4-}$ tetrahedron and $[\text{AlO}_4]^{5-}$ tetrahedron decreases and that the structure becomes less ordered [38].

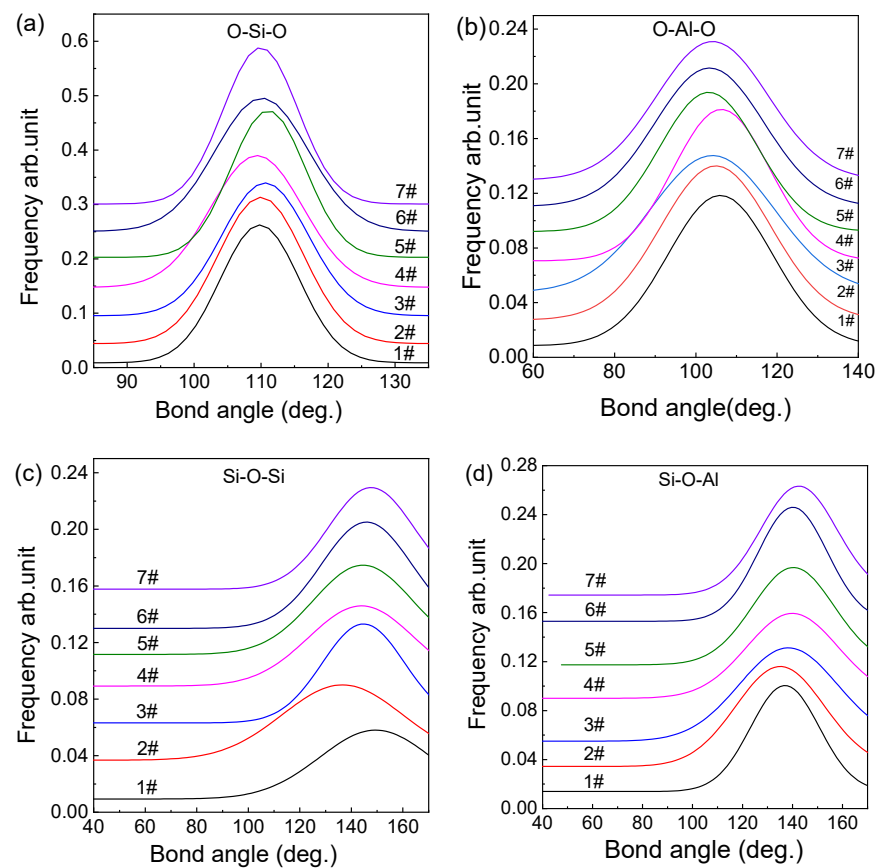


Figure 4. Distribution of bond angles of (a) O–Si–O, (b) O–Al–O, (c) Al–O–Al, and (d) Al–O–Si.

3.3. Distribution of Oxygen and Q^n

The tetrahedral structures of the network are not connected by edges or faces, only by corners. The oxygen at the shared corner is the BO, which connects two tetrahedral structures. The oxygen in a tetrahedral structure but not connected to other tetrahedral structures is a nonbridging oxygen (NBO) [21,26,37]. The network structure of fused red mud consists of different tetrahedral structures. Si^{4+} , Al^{3+} , Ti^{4+} , and Fe^{3+} ions can form $[\text{SiO}_4]^{4-}$ and $[\text{AlO}_4]^{5-}$ tetrahedral, $[\text{TiO}_6]^{8-}$ octahedron, and $[\text{FeO}_4]^{5-}$ tetrahedral structures with oxygen [36], respectively. Si and Al are network formers, and their ionic groups $[\text{SiO}_4]^{4-}$ and $[\text{AlO}_4]^{5-}$ are the main components of the network.

Figure 5 shows the distribution of BO and NBO of molten red mud with different $\text{SiO}_2/\text{Al}_2\text{O}_3$ mass ratios. Figure 5a shows that when the ratio of $\text{SiO}_2/\text{Al}_2\text{O}_3$ is small, the concentration of BO follows the order $\text{Si-O-Al} > \text{Al-O-Al} > \text{Si-O-Si}$. As the ratio of $\text{SiO}_2/\text{Al}_2\text{O}_3$ increases, the concentration of Si-O-Si BO increases correspondingly, and the concentration of Al-O-Al BO decreases rapidly, whereas the concentration of Si-O-Al BO first increases and then decreases. Figure 5b shows that with increasing $\text{SiO}_2/\text{Al}_2\text{O}_3$ ratio, the concentrations of Si-O-Ca NBO, Si-O-Mg NBO, and Al-O-Na NBO increase slightly, and the concentrations of the rest NBOs are almost unchanged.

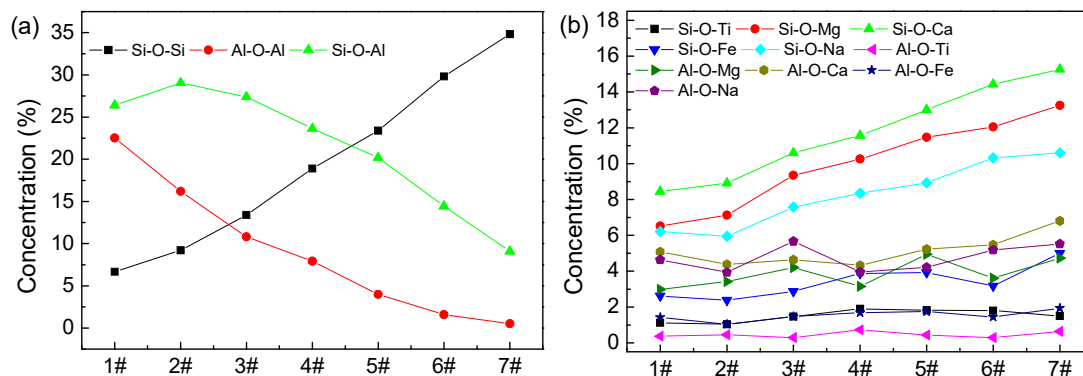


Figure 5. Distribution of BO and NBO in molten red mud: (a) BO and (b) NBO.

This phenomenon conforms to the Al avoidance principle [38]; i.e., Si-O-Al has the lowest bond energy, followed by Si-O-Si , and Al-O-Al has the highest bond energy. When the ratio of $\text{SiO}_2/\text{Al}_2\text{O}_3$ is small, the content of Si^{2+} in the molten red mud is low, and the content of Al^{3+} is high. As the Si^{2+} content increases, more Si-O-Al bonds are formed in the melt according to the Al avoidance principle. With increasing Si^{2+} and decreasing Al^{3+} , there is insufficient Al^{3+} in the melt to form Si-O-Al bonds. As a result, the content of Si-O-Al begins to decrease, thereby accelerating the formation of the Si-O-Si bonds.

Figure 6 shows the distribution of Q_m^n in $[\text{SiO}_4]$ and $[\text{AlO}_4]$ tetrahedra, where m ($m = \text{Si}, \text{Al}$) represents the atoms connected to BO in the $[\text{SiO}_4]^{4-}/[\text{AlO}_4]^{5-}$ tetrahedra and n represents the number of Bos in each $[\text{SiO}_4]^{4-}/[\text{AlO}_4]^{5-}$ tetrahedron. Figure 6a shows that, as the $\text{SiO}_2/\text{Al}_2\text{O}_3$ ratio increases, the concentrations of Q_{Si}^0 and Q_{Si}^1 in the $[\text{SiO}_4]^{4-}$ tetrahedra gradually decrease, the concentration of Q_{Si}^2 first increases and then decreases, and the concentrations of Q_{Si}^3 and Q_{Si}^4 gradually increase. In addition, Q_{Si}^4 is produced only in a small amount when the ratio of $\text{SiO}_2/\text{Al}_2\text{O}_3$ is 1.4.

Figure 6b shows that as the $\text{SiO}_2/\text{Al}_2\text{O}_3$ ratio increases, the Q_{Al}^0 concentration in the $[\text{SiO}_4]$ tetrahedra first changes slowly and then increases rapidly; the concentration of Q_{Al}^1 first increases and then decreases; and the concentrations of Q_{Al}^2 and Q_{Al}^3 first change slowly and then decrease rapidly. The amount of Q_{Al}^4 is very small. Moreover, Q_{Al}^4 disappears when the ratio of $\text{SiO}_2/\text{Al}_2\text{O}_3$ is greater than 3.

As shown in Figure 6c, with increasing $\text{SiO}_2/\text{Al}_2\text{O}_3$ ratio, the Q_{Al}^0 concentration in the $[\text{AlO}_4]^{5-}$ tetrahedra increases rapidly from the initial 17.44% to 76%. However, the concentrations of Q_{Al}^1 and Q_{Al}^2 increase first and then decrease; the amount of Q_{Al}^4 remains very small and disappears when the $\text{SiO}_2/\text{Al}_2\text{O}_3$ ratio is greater than 3.

As shown in Figure 6d, Q_{Si}^0 and Q_{Si}^1 are the main species in the $[\text{AlO}_4]^{5-}$ tetrahedra. With increasing $\text{SiO}_2/\text{Al}_2\text{O}_3$ ratio, the concentration of Q_{Si}^0 decreases from 83.1% to 68%, while the concentration of Q_{Si}^1 increases from 15.1% to 30%. The amounts of Q_{Si}^2 , Q_{Si}^3 , and Q_{Si}^4 remain very small and are minimally affected by the ratio of $\text{SiO}_2/\text{Al}_2\text{O}_3$.

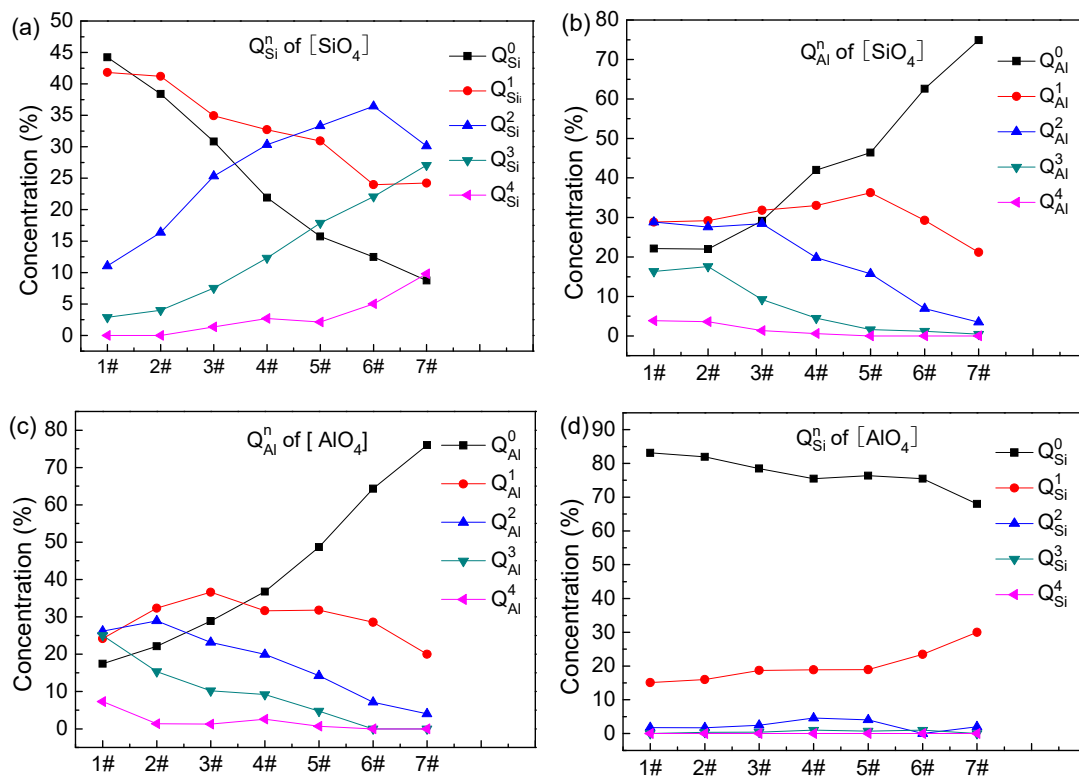


Figure 6. Distribution of Q^n species: (a,c) $[\text{SiO}_4]$ tetrahedron, (b,d) $[\text{AlO}_4]$ tetrahedron.

3.4. Self-Diffusion Coefficient and Viscosity

The atoms in the molten red mud are always moving, and the movement of each atom directly affects the viscosity of the melt. Viscosity is a critical parameter for the preparation of fibers using fused red mud and can directly affect the quality of the fibers. The mean square displacement (MSD) of the particles was calculated by analyzing the trajectories of the particles using the molecular dynamics method, and the self-diffusion coefficient of each atom was obtained by combining with the Einstein diffusion equation [39], as shown in Equations (4) and (5):

$$MSD = \langle \Delta r(t)^2 \rangle = \frac{1}{N} \left\langle \sum_{i=1}^N |r_{i(t)} - r_{i(0)}|^2 \right\rangle \quad (4)$$

where $r_{i(0)}$ is the position vector of atom i at time 0; $r_{i(t)}$ is the position vector of atom i at time t ;

$$D = \lim_{t \rightarrow \infty} \frac{1}{6} \frac{d[\Delta \bar{r}(t)^2]}{dt} = \lim_{t \rightarrow \infty} \frac{1}{6} \frac{d[MSD]}{dt} \quad (5)$$

Figure 7 shows the typical MSD curves as a function of time. Figure 6 shows the effect of $\text{SiO}_2/\text{Al}_2\text{O}_3$ mass ratios on the diffusion coefficient of each atom in the fused red mud system. Figure 8 shows that the ratio of $\text{SiO}_2/\text{Al}_2\text{O}_3$ has different effects on the diffusion of different atoms. The D_{Mg} value of Mg is much larger than those of other atoms and decreases with increasing $\text{SiO}_2/\text{Al}_2\text{O}_3$ ratio. As the $\text{SiO}_2/\text{Al}_2\text{O}_3$ ratio increases, D_{Ti} first decreases, then increases, and finally decreases again; whereas D_{Fe} remains unchanged at first, then rapidly decreases, and finally stabilizes. The diffusion coefficients of the remaining atoms decrease slowly with increasing $\text{SiO}_2/\text{Al}_2\text{O}_3$ ratio and follow the order $D_{Na} > D_{Ca} > D_{Al} > D_O > D_{Si}$. Mg is mainly present in the gaps of the network structure formed by silicon and aluminum. It is a network modifier and does not participate in the formation of the network. Thus, Mg can move in a large area, facilitating its diffusion. As for Ti, part of the Ti^{4+} can combine with O^{2-} to form $[\text{TiO}_6]^{8-}$ octahedron and participate in the formation of network structure. When the content of Al_2O_3 in the system is relatively

high, Ti^{4+} is mainly present in the gaps of the network structure and has high diffusivity. When the content of Al_2O_3 decreases and the content of SiO_2 is low, part of Ti^{4+} combines with O^{2-} to form $[TiO_6]^{8-}$ octahedron and participates in network formation, resulting in decreased D_{Ti} value. However, as the amount of SiO_2 increases, the binding between Si^{4+} and O^{2-} is stronger than that between Ti^{4+} and O^{2-} , so Ti^{4+} is squeezed out of the network structure, leading to an increase in its MSD. With the further addition of SiO_2 and decrease in Al_2O_3 , the viscosity of the system increases, resulting in difficulty in the migration of Ti^{4+} and thereby a decrease in MSD. Similarly, the Fe^{3+} in the gaps of the network structure also has strong diffusivity. Moreover, some Fe^{3+} participates in the formation of the silicate network to form $[FeO_4]$, reducing the movement range of Fe^{3+} . As the ratio of SiO_2/Al_2O_3 increases, the content of Si^{2+} in the system increases. The binding between Si^{4+} and O^{2-} is stronger than that between Fe^{3+} and O^{2-} , so Fe^{3+} is squeezed out of the network structure, resulting in an increase in its D value. However, as the ratio of SiO_2/Al_2O_3 further increases, more $[SiO_4]$ tetrahedra are formed, and the network becomes more complete. The viscosity of the system increases accordingly, the migration of Fe^{3+} is restricted, and its D value decreases. Si^{4+} and Al^{3+} combine with O^{2-} to form $[SiO_4]^{4-}$ and $[AlO_4]^{5-}$ tetrahedral structures. They are network formers and do not easily diffuse.

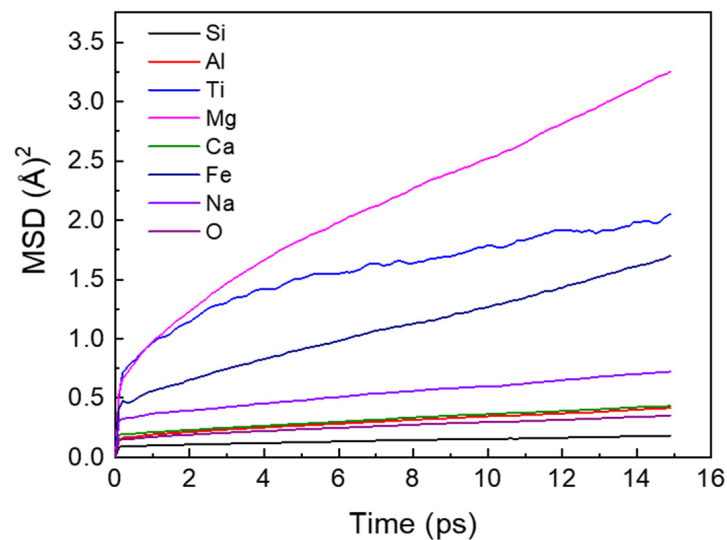


Figure 7. MSD curves for the #1 fused red mud system.

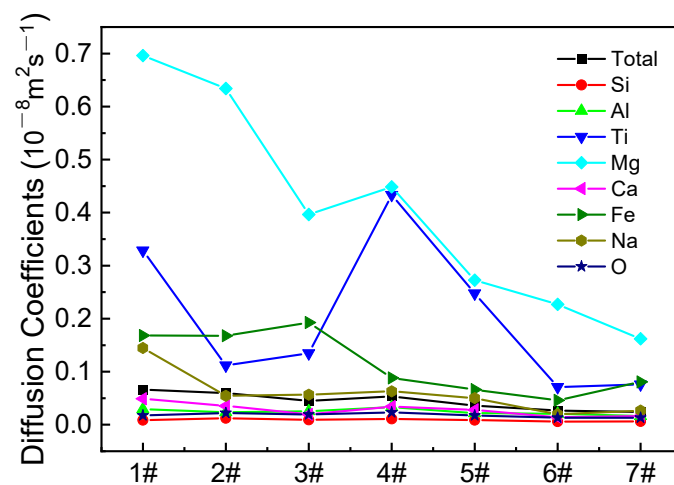


Figure 8. Effect of SiO_2/Al_2O_3 ratio on diffusion coefficients.

Equations relating viscosity to diffusivity have been widely used in the study of silicate melts [26,31,40], and the two most popular equations are the Eyring equation and the Stokes–Einstein equation. They were derived in different ways but relate diffusivity and viscosity through the same formula, as shown in Equation (6).

$$\eta = \frac{K_B T}{D\lambda} \quad (6)$$

where η is the viscosity coefficient, $\text{J}\cdot\text{m}^{-1}\cdot\text{s}$; K_B is the Boltzmann constant; T is the T_{end} , K; and $\lambda = 2R$, where R is the average diffusion distance of ions, Å. Based on this, the viscosity of the molten red mud is calculated by the total diffusion coefficient of the ions in the system. Figure 9 shows the effect of $\text{SiO}_2/\text{Al}_2\text{O}_3$ ratio on the viscosity and the total diffusion coefficient of molten red mud, the orange red histogram and blue curve in the figure represent the change of viscosity η and total diffusion coefficient D_{Total} , respectively, as can be seen from the figure, with the increasing SiO_2 , the viscosity first increase, then decrease slightly, and finally increase again. Conversely, the change of total diffusion coefficient is opposite. As discussed above, the bonding between Si^{4+} and O^{2-} is stronger than that between Ti^{4+} and O^{2-} or Fe^{3+} and O^{2-} . When the content of SiO_2 is low, part of Ti^{4+} and Fe^{3+} combines with O^{2-} to form $[\text{TiO}_6]$ octahedron and $[\text{FeO}_4]$ tetrahedra, respectively, and participate in network formation resulting in decreased the values of D_{Total} . However, with the gradual increase of Si^{4+} , Ti^{4+} and Fe^{3+} are squeezed out of the network structure, at this time, Ti^{4+} and Fe^{3+} have strong diffusivity, leading to an increase in its D_{Total} and decrease in its viscosity, as show in Figure 9. When the $\text{SiO}_2/\text{Al}_2\text{O}_3$ ratio increases from 1.4 (3# sample) to 2 (4# sample), D_{Total} value increase from $4.5 \times 10^{-10} \text{ m}^2\text{s}^{-1}$ to $5.3 \times 10^{-10} \text{ m}^2\text{s}^{-1}$, correspondingly, the viscosity η value drops from 1.27 Pa·s to 1.06 Pa·s. However, as the amount of Si^{2+} in the melt further increases, more $[\text{SiO}_4]$ tetrahedra are formed, the degree of polymerization of the network is higher, the diffusion of Ti^{4+} and Fe^{3+} is limited again, and the D_{Total} becomes smaller, from $5.3 \times 10^{-10} \text{ m}^2\text{s}^{-1}$ (4# sample) to $2.4 \times 10^{-10} \text{ m}^2\text{s}^{-1}$ (7# sample), correspondingly, the η increases again, from 1.06 Pa·s to 2.37 Pa·s.

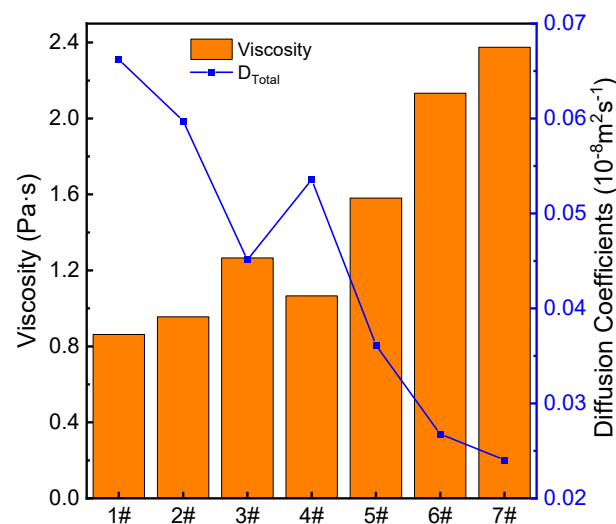


Figure 9. Effect of $\text{SiO}_2/\text{Al}_2\text{O}_3$ ratio on viscosity and total diffusion coefficients.

4. Conclusions

The effect of $\text{SiO}_2/\text{Al}_2\text{O}_3$ mass ratio on the structural properties and viscosity of the molten fused red mud were systematically analyzed by the molecular dynamics method. The conclusions are as follows:

1. The average bond lengths of Si–O, Al–O, Ca–O, Mg–O, Na–O, Ti–O, and Fe–O are 1.59 Å, 1.79 Å, 2.31 Å, 2.29 Å, 2.33 Å, 2.45 Å, and 2.51 Å, respectively. The network formers of the fused red mud are $[\text{SiO}_4]$ and $[\text{AlO}_4]$ tetrahedra.
2. With increasing $\text{SiO}_2/\text{Al}_2\text{O}_3$ ratio, the concentration of Si–O–Si BO in the molten red mud increases, the concentration of Al–O–Al BO decreases, and the concentration of Si–O–Al BO first increases and then decreases; the concentrations of Si–O–Ca NBO, Si–O–Mg NBO, and Si–O–Na NBO increase, and the remaining NBOs do not change significantly.
3. The average bond angles of O–Si–O, O–Al–O, Si–O–Si, and Al–O–Si in the fused red mud are 110.2° , 106.5° , 144.5° , and 138.9° , respectively. With increasing $\text{SiO}_2/\text{Al}_2\text{O}_3$ ratio, the peaks of O–Si–O and Si–O–Si bond angle distributions become narrower, while the peaks of O–Al–O and Al–O–Si become wider. The results indicate that the degree of polymerization of $[\text{SiO}_4]$ tetrahedral network increases and that the degree of polymerization of $[\text{AlO}_4]$ tetrahedra decreases, leading to a more compact melt structure.
4. With increasing $\text{SiO}_2/\text{Al}_2\text{O}_3$ ratio, (1) in the distribution of Q_{Si}^n of $[\text{SiO}_4]$, Q_{Si}^0 and Q_{Si}^1 decrease, and Q_{Si}^2 first increases and then decreases; (2) in the distribution of Q_{Al}^n of $[\text{SiO}_4]$, Q_{Al}^0 increases, Q_{Al}^1 first increases and then decreases, Q_{Al}^2 and Q_{Al}^3 first change slowly and then decrease, and the content of Q_{Al}^4 is very small and goes to zero when the ratio of $\text{SiO}_2/\text{Al}_2\text{O}_3$ is greater than 3; (3) the concentration of Q_{Al}^0 in the $[\text{AlO}_4]$ tetrahedra increases rapidly from the initial 17.44% to 76%, Q_{Al}^1 and Q_{Al}^2 first increase and then decrease, the content of Q_{Al}^4 remains very small and goes to zero when the ratio of $\text{SiO}_2/\text{Al}_2\text{O}_3$ is greater than 3; and (4) the concentration of Q_{Si}^0 in the $[\text{AlO}_4]$ tetrahedra decreases from 83.1% to 68%, while the concentration of Q_{Si}^1 increases from 15.1% to 30%, and the concentrations of Q_{Si}^2 , Q_{Si}^3 , and Q_{Si}^4 remain very small and are minimally influenced by the $\text{SiO}_2/\text{Al}_2\text{O}_3$ ratio.
5. With increasing $\text{SiO}_2/\text{Al}_2\text{O}_3$ ratio, the viscosity of the fused red mud first increases, then decreases, and finally increases because Ti^{4+} and Fe^{3+} combine with O^{2-} to form $[\text{TiO}_4]$ octahedron and $[\text{FeO}_4]$ tetrahedra, which increase the degree of polymerization of the melt.

Author Contributions: Y.L. and B.X. performed theoretical analysis and wrote the article; Y.C. and Z.W. performed the simulation calculations; and P.D. helped with data collation. All authors have read and agreed to the published version of the manuscript.

Funding: This study was funded by the China National Natural Science Foundation Regional Innovation and Development Joint Fund (Grant No. U20A20271) and the China National Natural Science Foundation General Program (Project No. 51874138).

Data Availability Statement: Data of this study are available on request from the corresponding authors.

Conflicts of Interest: The authors declare no conflict of interest.

References

1. Lima, M.S.; Thives, L.P. Evaluation of red mud as filler in Brazilian dense graded asphalt mixtures. *Constr. Build. Mater.* **2020**, *260*, 119894. [\[CrossRef\]](#)
2. Lu, G.-Z.; Zhang, T.-A.; Ma, L.-N.; Wang, Y.-X.; Zhang, W.-G.; Zhang, Z.-M.; Wang, L. Utilization of Bayer red mud by a calcification–carbonation method using calcium aluminate hydrate as a calcium source. *Hydrometallurgy* **2018**, *188*, 248–255. [\[CrossRef\]](#)
3. Mukiza, E.; Zhang, L.; Liu, X.; Zhang, N. Utilization of red mud in road base and subgrade materials: A review. *Resour. Conserv. Recycl.* **2018**, *141*, 187–199. [\[CrossRef\]](#)
4. Ma, J.; Wang, M.; You, J.; Tang, K.; Lu, L.; Wan, S.; Wang, J.; Gong, X.; Wang, Y. Quantitative studies on the structure of $x\text{CaO}\cdot(1-x)\text{SiO}_2$ glasses and melts by in-situ Raman spectroscopy, ^{29}Si MAS NMR and quantum chemistry ab initio calculation. *J. Non-Cryst. Solids* **2020**, *546*, 1–9. [\[CrossRef\]](#)
5. Wang, C.; Li, Z.; Zhou, Z.; Gao, Y.; Zhang, J. Compatibility of different fibres with red mud-based geopolymer grouts. *Constr. Build. Mater.* **2022**, *315*, 125742. [\[CrossRef\]](#)

6. Ding, C.; Zhang, Y.; Zhang, N.; Di, X.; Li, Y.; Zhang, Y. A new insight into utilization of red mud in poly(vinyl chloride) composites via surface modification and toughening modulation to attain performance optimization. *Constr. Build. Mater.* **2022**, *333*, 127340. [[CrossRef](#)]
7. Hou, D.; Wu, D.; Wang, X.; Gao, S.; Yu, R.; Li, M.; Wang, P.; Wang, Y. Sustainable use of red mud in ultra-high performance concrete (UHPC): Design and performance evaluation. *Cem. Concr. Compos.* **2020**, *115*, 103862. [[CrossRef](#)]
8. Zhang, J.; Yao, Z.; Wang, K.; Wang, F.; Jiang, H.; Liang, M.; Wei, J.; Airey, G. Sustainable utilization of bauxite residue (Red Mud) as a road material in pavements: A critical review. *Constr. Build. Mater.* **2020**, *270*, 121419. [[CrossRef](#)]
9. Kan, L.; Wang, F. Mechanical properties of high ductile alkali-activated fiber reinforced composites incorporating red mud under different curing conditions. *Ceram. Int.* **2022**, *48*, 1999–2011. [[CrossRef](#)]
10. Vigneshwaran, S.; Uthayakumar, M.; Arumugaprabu, V. Development and sustainability of industrial waste-based red mud hybrid composites. *J. Clean. Prod.* **2019**, *230*, 862–868. [[CrossRef](#)]
11. Kim, Y.; Kim, M.; Sohn, J.; Park, H. Applicability of gold tailings, waste limestone, red mud, and ferronickel slag for producing glass fibers. *J. Clean. Prod.* **2018**, *203*, 957–965. [[CrossRef](#)]
12. Qiu, G.; Miao, D.; Wei, X.; Bai, C.; Li, X. Effect of MgO/Al₂O₃ and CaO/SiO₂ on the Metallurgical Properties of CaO-SiO₂-Al₂O₃-MgO-TiO₂ Slag. *J. Non-Cryst. Solids* **2022**, *585*, 1–10. [[CrossRef](#)]
13. Ma, H.; Jiao, K.; Zhang, J.; Zong, Y.; Zhang, J.; Meng, S. Viscosity of CaO-MgO-Al₂O₃-SiO₂-TiO₂-FeO slag with varying TiO₂ content: The Effect of Crystallization on Viscosity Abrupt Behavior. *Ceram. Int.* **2021**, *47*, 17445–17454. [[CrossRef](#)]
14. Liu, W.; Zuo, H. Effect of MnO and CaO substitution for BaO on the viscosity and structure of CaO-SiO₂-MgO-Al₂O₃-BaO-MnO slag. *J. Non-Cryst. Solids* **2021**, *567*, 1–8. [[CrossRef](#)]
15. Liu, W.; Qin, J.; Xing, X.; Wang, J.; Zuo, H. Viscosity and structure evolution of CaO-SiO₂-MgO-Al₂O₃-BaO slag with the CaO/SiO₂ mass ratio of 0.9. *Ceram. Int.* **2021**, *47*, 33483–33489. [[CrossRef](#)]
16. Feng, C.; Gao, L.-H.; Tang, J.; Liu, Z.-G.; Chu, M.-S. Effects of MgO/Al₂O₃ ratio on viscous behaviors and structures of MgO-Al₂O₃-TiO₂-CaO-SiO₂ slag systems with high TiO₂ content and low CaO/SiO₂ ratio. *Trans. Nonferr. Metal. Soc.* **2020**, *30*, 800–811. [[CrossRef](#)]
17. Sun, Y.; Chen, M.; Zhao, B. Modification of the microstructures of CaO-SiO₂-Al₂O₃-MgO slags using various minor elements. *J. Non-Cryst. Solids* **2019**, *515*, 50–57. [[CrossRef](#)]
18. Deng, L.; Zhang, X.; Zhang, M.; Jia, X. Effect of CaF₂ on viscosity, structure and properties of CaO-Al₂O₃-MgO-SiO₂ slag glass ceramics. *J. Non-Cryst. Solids* **2018**, *500*, 310–316. [[CrossRef](#)]
19. Zhang, S.; Zhang, X.; Liu, W.; Lv, X.; Bai, C.; Wang, L. Relationship between structure and viscosity of CaO-SiO₂-Al₂O₃-MgO-TiO₂ slag. *J. Non-Cryst. Solids* **2014**, *402*, 214–222. [[CrossRef](#)]
20. Mongalo, L.; Lopis, A.S.; Venter, G.A. Molecular dynamics simulations of the structural properties and electrical conductivities of CaO-MgO-Al₂O₃-SiO₂ melts. *J. Non-Cryst. Solids* **2016**, *452*, 194–202. [[CrossRef](#)]
21. Zhao, H.; Li, J.; Yang, S.; Liu, J.; Liu, W. Molecular Dynamics Study of Structural Properties of Refining Slag with Various CaO/Al₂O₃ Ratios. *Minerals* **2021**, *11*, 398. [[CrossRef](#)]
22. Jiang, C.; Li, K.; Zhang, J.; Liu, Z.; Niu, L.; Liang, W.; Sun, M.; Ma, H.; Wang, Z. The effect of CaO and MgO on the structure and properties of coal ash in the blast furnace: A molecular dynamics simulation and thermodynamic calculation. *Chem. Eng. Sci.* **2019**, *210*, 115226. [[CrossRef](#)]
23. Gao, L.; Liu, X.; Bai, J.; Kong, L.; Bai, Z.; Li, W. Structure and flow properties of coal ash slag using ring statistics and molecular dynamics simulation: Role of CaO/Na₂O in SiO₂-Al₂O₃-CaO-Na₂O. *Chem. Eng. Sci.* **2021**, *231*, 116285. [[CrossRef](#)]
24. Dai, X.; Bai, J.; Huang, Q.; Liu, Z.; Bai, X.; Lin, C.-T.; Li, W.; Guo, W.; Wen, X.; Du, S. Coal ash fusion properties from molecular dynamics simulation: The role of calcium oxide. *Fuel* **2018**, *216*, 760–767. [[CrossRef](#)]
25. Atila, A.; Ghardi, E.M.; Hasnaoui, A.; Ouaskit, S. Alumina effect on the structure and properties of calcium aluminosilicate in the percalcic region: A molecular dynamics investigation. *J. Non-Cryst. Solids* **2019**, *525*, 1–14. [[CrossRef](#)]
26. Chen, Y.; Pan, W.; Jia, B.; Wang, Q.; Zhang, X.; Wang, Q.; He, S. Effects of the amphoteric behavior of Al₂O₃ on the structure and properties of CaO-SiO₂-Al₂O₃ melts by molecular dynamics. *J. Non-Cryst. Solids* **2021**, *552*, 120435. [[CrossRef](#)]
27. Jabraoui, H.; Badawi, M.; Lebègue, S.; Vaills, Y. Elastic and structural properties of low silica calcium aluminosilicate glasses from molecular dynamics simulations. *J. Non-Cryst. Solids* **2018**, *499*, 142–152. [[CrossRef](#)]
28. Kim, T.S.; Park, J.H. Thermodynamics of iron redox equilibria and viscosity-structure relationship of CaO-Al₂O₃-FeO melts. *J. Non-Cryst. Solids* **2020**, *542*, 1–9. [[CrossRef](#)]
29. Zhao, Y.; Du, J.; Qiao, X.; Cao, X.; Zhang, C.; Xu, G.; Liu, Y.; Peng, S.; Han, G. Ionic self-diffusion of Na₂O-Al₂O₃-SiO₂ glasses from molecular dynamics simulations. *J. Non-Cryst. Solids* **2020**, *527*, 1–9. [[CrossRef](#)]
30. Jiang, C.; Li, K.; Zhang, J.; Qin, Q.; Liu, Z.; Sun, M.; Wang, Z.; Liang, W. Effect of MgO/Al₂O₃ ratio on the structure and properties of blast furnace slags: A molecular dynamics simulation. *J. Non-Cryst. Solids* **2018**, *502*, 76–82. [[CrossRef](#)]
31. Wu, T.; Wang, Q.; Yu, C.; He, S. Structural and viscosity properties of CaO-SiO₂-Al₂O₃-FeO slags based on molecular dynamic simulation. *J. Non-Cryst. Solids* **2016**, *450*, 23–31. [[CrossRef](#)]
32. Wu, T.; He, S.; Liang, Y.; Wang, Q. Molecular dynamics simulation of the structure and properties for the CaO-SiO₂ and CaO-Al₂O₃ systems. *J. Non-Cryst. Solids* **2015**, *411*, 145–151. [[CrossRef](#)]
33. Zhang, S.; Zhang, X.; Bai, C.; Wen, L.; Lv, X. Effect of TiO₂ Content on the Structure of CaO-SiO₂-TiO₂ System by Molecular Dynamics Simulation. *ISIJ Int.* **2013**, *53*, 1131–1137. [[CrossRef](#)]

34. Shimoda, K.; Saito, K. Detailed Structure Elucidation of the Blast Furnace Slag by Molecular Dynamics Simulation. *ISIJ Int.* **2007**, *47*, 1275–1279. [[CrossRef](#)]
35. Okuno, M.; Kawamura, K. Molecular dynamics calculations for $Mg_3Al_2Si_3O_{12}$ (pyrope) and $Ca_3Al_2Si_3O_{12}$ (grossular) glass structures. *J. Non-Cryst. Solids* **1995**, *191*, 249–259. [[CrossRef](#)]
36. Goj, P.; Stoch, P. Molecular dynamics simulations of P_2O_5 - Fe_2O_3 - FeO - Na_2O glasses. *J. Non-Cryst. Solids* **2018**, *500*, 70–77. [[CrossRef](#)]
37. Wu, T.; Wang, Q.; Yao, T.; He, S. Molecular dynamics simulations of the structural properties of Al_2O_3 -based binary systems. *J. Non-Cryst. Solids* **2016**, *435*, 17–26. [[CrossRef](#)]
38. Lee, S.K.; Stebbins, J.F. Al-O-Al and Si-O-Si sites in framework aluminosilicate glasses with Si/Al = 1: Quantification of framework disorder. *J. Non-Cryst. Solids* **2000**, *270*, 260–264. [[CrossRef](#)]
39. Nevins, D.; Spera, F.J.; Ghiorso, M.S. Shear viscosity and diffusion in liquid $MgSiO_3$: Transport properties and implications for terrestrial planet magma oceans. *Am. Miner.* **2009**, *94*, 975–980. [[CrossRef](#)]
40. Avid, T.; Charles, E.L.; Gregory, M.B.; Takeyuki, U.; Wang, Y. High-pressure viscometry of polymerized silicate melts and limitations of the Eyring equation. *Am. Miner.* **2004**, *89*, 1701–1708.